



Sodium doping and 3D honeycomb nanoarchitecture: Key features of covalent triazine-based frameworks (CTF) organocatalyst for enhanced solar-driven advanced oxidation processes

Tao Zeng^{a,b}, Shuqi Li^a, Yi Shen^a, Haiyan Zhang^a, Hongru Feng^c, Xiaole Zhang^d, Lingxiangyu Li^e, Zongwei Cai^{b,*}, Shuang Song^{a,*}

^a Key Laboratory of Microbial Technology for Industrial Pollution Control of Zhejiang Province, College of Environment, Zhejiang University of Technology, Hangzhou, Zhejiang, 310032, PR China

^b State Key Laboratory of Environmental and Biological Analysis, Department of Chemistry, Hong Kong Baptist University, Hong Kong, China

^c State Key Laboratory of Environmental Chemistry and Ecotoxicology, Research Center for Eco-Environmental Sciences, Chinese Academy of Sciences, Beijing, 100085, PR China

^d College of Life Science, North China University of Science and Technology, Tangshan, Hebei, 063000, PR China

^e Department of Chemistry, School of Sciences, Zhejiang Sci-Tech University, Hangzhou, 310018, PR China

ARTICLE INFO

Keywords:

Sodium-doped CTFs
3D honeycomb nanoarchitecture
Visible-light harvesting
Peroxymonosulfate
Oxidation degradation.

ABSTRACT

Herein, we designed a novel sodium-doped covalent triazine-based framework with a 3D honeycomb nanoarchitecture (H-CTF-Na) as visible-light-responsive organocatalyst to efficiently drive advanced oxidation processes (AOPs). Experimental and theoretical findings reveal that Na doping narrows the band gap by elevating the band edges and the 3D hierarchical nanocellular morphology improves light harvesting and electron transfer. With these merits, H-CTF-Na showed a photoactivity enhancement of 4.9–6.0-fold for the degradation of carbamazepine (CBZ) compared to those of pristine CTFs and g-C₃N₄ through peroxymonosulfate (PMS) activation under visible-light irradiation. The quenching and EPR results indicate that a synergistic effect between photooxidation (h^+) and PMS activation ($^{\bullet}\text{OH}$ and $\text{SO}_4^{\bullet-}$) derived from the vigorous capture of photogenerated e^- by PMS is responsible for the marked efficacy of H-CTF-Na/vis/PMS system. Moreover, this system exhibited excellent versatility in degrading other organics (such as various phenols and dyes) and good reusability in terms of five high-efficiency recycled uses.

1. Introduction

Water contamination caused by the ceaseless discharge of organic pollutants is one of the major problems faced by modern society, and tremendous efforts have been devoted to developing advanced technology for addressing this environmental issue [1–3]. Recently, increasing attention has been drawn toward peroxymonosulfate (PMS)-mediated advanced oxidation processes (AOPs) to develop efficient and environmentally friendly strategy for water purification [4–7]. Such systems rely on PMS activation to generate highly reactive sulfur species (e.g., sulfate radical ($\text{SO}_4^{\bullet-}$)) and oxygen species (ROS, e.g., hydroxyl radical ($^{\bullet}\text{OH}$) and singlet oxygen ($^1\text{O}_2$)) through various strategies, including UV irradiation, ultrasound, electrochemical methods, and inorganic heterogeneous nanocatalysts [8–14]. Unfortunately, most of the current methods suffer from inherent defects such as the essential high cost caused by additional energy inputs in the activation

process and the potential secondary contamination due to the release of transition metal from normal inorganic catalysts [15–18]. Even for metal-free nanocarbons, the performance in activating PMS and durability are consistently low, and high temperatures (generally above 800 °C) are often required for synthesis [19–21]. Therefore, a novel PMS activation strategy satisfying the combined requirements of low cost, high stability and efficiency remains a long-term goal for realizing practical applications.

Visible-light-responsive polymers appear to be attractive alternatives to conventional PMS activators because of not only the advantages of cost effectiveness, tunable properties, and ease of synthesis, but also their ability to directly harvest inexpensive and renewable solar energy [22–25]. In addition, the involvement of PMS in photocatalysis could introduce an electron acceptor to capture photo-generated electrons and thus accelerate the charges separation, which, in turn, expedites photooxidation reactions [26–28]. However, this area

* Corresponding authors.

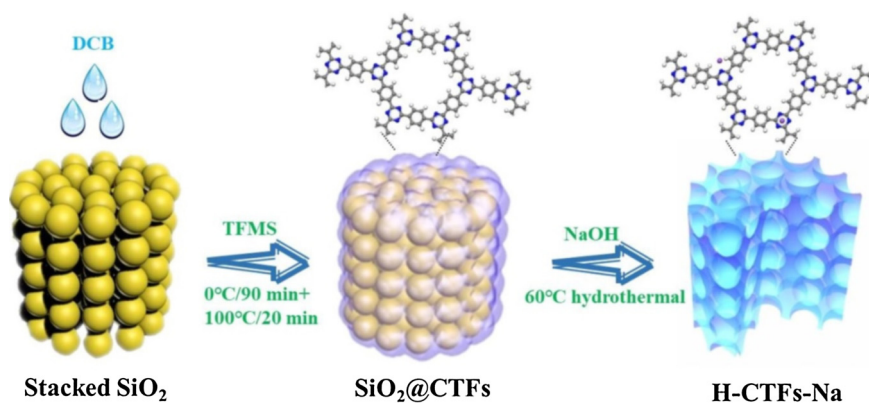
E-mail addresses: zwcai@hkbu.edu.hk (Z. Cai), ss@zjut.edu.cn (S. Song).

<https://doi.org/10.1016/j.apcatb.2019.117915>

Received 25 March 2019; Received in revised form 6 June 2019; Accepted 1 July 2019

Available online 02 July 2019

0926-3373/ © 2019 Elsevier B.V. All rights reserved.



Scheme 1. Schematic illustration of the fabrication of 3D H-CTFs-Na material.

remains relatively underexplored, although some progresses in design g-C₃N₄-based photocatalysts for PMS activation [29–34]. Most of the current g-C₃N₄-vis-PMS systems are still far from achieving satisfactory performance for practical applications, and more works are desirable to develop improved polymer photocatalysts.

As a new type of porous polymer sharing similar triazine units as g-C₃N₄, covalent triazine-based frameworks (CTFs) have recently attracted a great deal of interest in photocatalytic solar-energy conversion; [35–38] however, its application in environmental remediation is at its nascent stage. Theoretical calculations have shown that CTFs possess semiconductor characteristics with broad absorption in the visible range and thus have predicted the great potential of CTFs for solar-assisted handling environmental issues [39]. The limited utilization of CTFs in solar-driven AOPs is likely due to the limited visible-light utilization, fast charge recombination, and harsh synthesis condition [40–42]. To optimize the properties of CTFs, a few attempts found that chemical doping with alien atoms such as sulfur [43], phosphorus [44], and oxygen [45] could modify the electronic structure for improving the photocatalytic performance on hydrogen evolution or CO₂ reduction. Although these shed light on design CTFs materials with nonmetal doping, there is still considerable room for improvement in the synthesis and properties of them. For example, doping alkali metals into g-C₃N₄ has been found to be capable of improving the photocatalytic performance [46,47], but the evidence on the performance and underlying mechanism of CTFs doped with them remains scanty. In addition to the chemical environment regulation, nanoarchitecture control of CTFs is also an important tool for optimizing catalytic efficiency. Particularly, 3D ordered macroporous structure has been shown not only to produce numerous access channels for the mobility of photogenerated carriers and the transfer of reactant species, but also to increase light absorption efficiency via multiple light-scattering and reflection effects [48–50]. To date, however, searching an efficient strategy for the fabrication of 3D CTFs is a challenging task, since the CTFs obtained from common synthetic methods usually grain with bulk/sheet structure which lacks of flexibility to well integrate with templates.

With these in mind, herein we employed an ultramild polymerization strategy to synthesize novel sodium-doped CTFs with 3D hierarchical honeycomb features (H-CTF-Na) and investigate its possible application as visible-light-responsive polymeric photocatalysts in PMS-mediated AOPs. A monomer of 1,4-dicyanobenzene was filled into the voids of SiO₂ nanoparticles, followed by a trifluoromethanesulfonic acid-initiated polymerization process to form CTFs. After further NaOH-assisted template-digesting treatment, a final H-CTF-Na with both a 3D honeycomb nanostructure and Na doping features was obtained. The prepared H-CTF-Na materials far outperformed benchmark catalysts (such as g-C₃N₄, pure CTFs, and CTF-Na) in carbamazepine degradation through PMS activation under visible-light irradiation. Such performance enhancement was proven to be caused by the following: I) Na-

doping extended visible-light absorption and narrowed the band gap of CTFs by changing the chemical environment; II) the 3D cavity-abundant nanocellular scaffold enabled multiple scattering and reflection of the incident light within the hollow cavity as well as quick light transmission to the surface, thus enhancing light harvesting and electron transfer; and III) involvement of PMS facilitated the separation of charge carriers by rapidly capturing photogenerated electrons, accompanied by production of highly reactive species. This work provides valuable insight for the design of optimized polymer photocatalysts and green remediation of contaminated water.

2. Experimental section

2.1. Chemicals

1,4-Dicyanobenzene (DCB), trifluoromethanesulfonic acid (TFMS), peroxymonosulfate (PMS, Oxone[®], 2KHSO₅·KHSO₄·K₂SO₄), 5,5-dimethyl-1-pyrroline-*N*-oxide (DMPO), and 2,2,6,6-tetramethylpiperidinyloxy (TEMP) were purchased from Sigma-Aldrich Chemical Co., Ltd. Tetraethyl orthosilicate (TEOS) and carbamazepine (CBZ) were obtained from Aladdin. Bisphenol A, phenol, 4-chlorophenol, Acid Orange 7, Rhodamine B, *Tert*-butyl alcohol (TBA), methanol (MeOH), ethanol (EtOH), disodium ethylenediaminetetraacetate (EDTA-2Na), and 2-*tert*-butyl-1,4-benzoquinone (*p*-BQ) were obtained from Sinopharm Chemical Reagent Co. Ltd. (Shanghai, China). Ammonium hydroxide (NH₃·H₂O, 25–28% NH₃ basis) was supplied by Hangzhou Longshan Fine Chemical Co., Ltd. (Hangzhou, China). All chemicals were used as received without any further purification. Ultrapure water was obtained from Milli-Q[®] Ultrapure Water Purification Systems (Milford, MA).

2.2. Synthesis of organocatalyst

The overall synthetic route involves three main steps (Scheme 1): Uniform silica microspheres were first prepared as template-honeycomb structure-directing agents according to a modified Stöber method [51]. Then, 4 mmol of DCB was dissolved in 2.5 mL of TFMS under nitrogen at 0 °C, followed by the addition of 0.5 g of silica microspheres to the viscous solution and further stirring for 1.5 h at 0 °C. After heating to 100 °C for 20 min, the resultant products (SiO₂@CTFs) were collected by centrifugation; washed with an ammonia solution, water and ethanol several times; and dried at 60 °C under vacuum overnight. Moreover, pristine CTFs were fabricated by the same procedure in the absence of SiO₂ templates. Finally, H-CTF-Na catalysts were facilely achieved by etching the silica cores (0.5 g SiO₂@CTFs) at 60 °C for 5 h under alkaline (0.5 M NaOH) hydrothermal conditions. The samples were collected by centrifugation, washed with ultra-pure water four times, and dried under vacuum at 60 °C for 12 h. For comparison, pristine CTFs were also treated under the same alkaline hydrothermal

conditions to obtain a Na-doped sample (CTF-Na).

2.3. Experimental procedure and analyses

The degradation of a typical pharmaceutical (CBZ) in water under visible-light irradiation in the presence of PMS was selected to test the activity of the catalysts. In a typical experiment, an aqueous solution of CBZ (100 mL, 5 mg L⁻¹) with an initial pH of 6.3 was mixed with PMS (1.3 mM) at 25 °C under magnetic stirring. A 300 W Xe lamp (PLS-SXE300; Beijing Perfect Light Co., Ltd, Beijing, China) with a 400 nm cutoff was selected as the visible-light source, and the reactions were triggered by adding 0.4 g L⁻¹ of catalysts to the abovementioned mixture. During the photocatalytic reaction, 1.0 mL aliquots were removed at different time intervals, followed by the addition of methanol to quench the radicals and filtration with a 0.22 µm organic phase filter to separate the supernatant from the catalysts for analysis. Other organics (i.e. bisphenol A, phenol, 4-chlorophenol, Acid Orange 7, and Rhodamine B) were degraded under conditions as following: organics, 100 µM; PMS, 0.65 mM; catalyst, 0.1 g L⁻¹. An HPLC system (Waters 1525) with a C₁₈ column (4.6 mm × 150 mm, 5 µm) and a UV detector was used to detect the CBZ concentration in the reaction mixture, with a column temperature of 35 °C and a detection wavelength of 285 nm. The mobile phase was methanol:water (70:30), and the flow rate was set to 1 mL min⁻¹. The mineralization grade of CBZ with/without PMS under visible-light irradiation was determined using a TOC analyzer (TOC-L Shimadzu, standard deviation < 0.2 mg L⁻¹). Radicals (SO₄^{•-}, HO[•] and O₂^{•-}) and singlet oxygen (¹O₂) were detected by electron paramagnetic resonance (EPR, EMX-10/12, Bruker, Germany) spectroscopy with 80.0 mM of DMPO and 5.0 mM of TEMP as the spin-trapping agent.

Other experiments, including characterizations, photoelectrochemical tests, analytical methods, and theoretical computations, are detailed in the Supporting Information.

3. Results and discussion

3.1. Characterization of materials

Unlike the traditional polymerization process for CTF synthesis (400 °C, ~40 h), the polymerization strategy used here (100 °C, ~2 h) was much milder and faster. The morphology and structure of various samples were characterized by scanning electron microscopy (SEM) and transmission electron microscopy (TEM). TEM revealed that the bulk CTF material appears as a flat slider (Fig. 1a). For SiO₂@CTFs (Fig. 1b), both the surface of the SiO₂ spheres (with a uniform diameter of ~150 nm) and the void space between them were tightly coated or filled with CTF polymer. After treatment with NaOH solution, hollow shells with thicknesses ranging from 10 nm to 30 nm clearly appeared because the SiO₂ spheres were completely etched and removed (Fig. 1c). Notably, no apparent collapse of the CTF polymer was observed after removing the template, suggesting a robust and rigid polymer skeleton. These hollow spheres were closely packed to form 3D conductive nanocellular scaffolds with efficient space-packing arrangements, which facilitates charge transfer and light harvesting. After treatment with the same alkaline hydrothermal process, the CTFs without the SiO₂ template showed no distinct difference in morphology compared with the pristine CTFs. EDX elemental mapping analysis confirmed the presence of C, N, and Na in the H-CTF-Na materials. The elements C and N originating from CTFs were homogeneously distributed in the as-prepared nanocellular scaffold, while the presence of Na affirmed successful doping during the NaOH hydrothermal treatment. STEM (Fig. 1d) and SEM images (Fig. 1e) revealed that the entire morphology of H-CTF-Na is very similar to that of a honeycomb (Fig. 1f), manifesting a 3D bioinspired hierarchical structure.

Fig. 2a shows the X-ray diffraction (XRD) patterns of various samples. For pristine CTFs, two main peaks at 15.9° and 25.7° were

detected, reflecting the (100) facet corresponding to the in-plane long-range molecular order of the polymer network and the (002) plane arising from the interlayer stacking of the π -conjugated rings, respectively [52]. For SiO₂@CTFs, three sharp diffraction peaks at 18.5°, 23° and 27° indicated the characteristic peaks of the silica matrix, demonstrating that SiO₂ spheres were successfully infiltrated by the CTF polymer. Interestingly, the two characteristic peaks of CTFs were well maintained in the patterns of CTF-Na and H-CTF-Na, accompanied by a shift of the (002) plane from 15.9° to 14.2°, indicating that the alkaline hydrothermal treatment did not notably destroy the periodic structure but merely caused a minute structural change. This shift could be interpreted as the incorporation of Na into the treated CTFs and the subsequent expansion of the lamellar spacing due to the larger radius of a Na ion compared to that of a C or N atom [53].

To certify the successful polymerization of nitrile monomer into triazine rings and the high stability during alkaline treatment, the products were examined by solid-state ¹³C NMR and Fourier transform infrared (FTIR) spectroscopy. As shown in Fig. 2b, the characteristic signal of sp²-hybridized carbon species appeared at approximately 120–140 ppm, and that of sp² carbon atoms in the triazine ring occurred at ~170 ppm. Signals located at 60 ppm could be ascribed to N-alkyl C.⁴¹ The NMR spectrum of H-CTF-Na is similar to that of the CTFs, indicating that no apparent structural decomposition occurred after alkaline treatment. Moreover, the NMR signal intensity of the H-CTF-Na sample increased slightly, possibly due to the high surface exposure derived from the unique 3D structure. The higher Brunauer–Emmett–Teller (BET) surface area of the H-CTF-Na catalyst compared to that of the pristine CTFs supports this possibility (Table S1). In the FTIR spectra (Fig. 2c), absorption peaks at 750–810 cm⁻¹ and 1330–1600 cm⁻¹ were observed for all products and correspond to the breathing mode of the triazine units and vibrational stretching modes of aromatic C=N bonds, which supports the formation of triazine rings [54]. After alkaline treatment, the strong absorption band centered at 1100 cm⁻¹ for Si-O bonds disappeared as a result of the removal of template. In addition, the weak signal at 2220 cm⁻¹ for typical terminal cyano groups of CTFs entirely vanished after hydrothermal treatment, which is conducive to reducing the number of defects as charge recombination centers.

X-ray photoelectron spectroscopy (XPS) was further employed to analyze the chemical states and composition. The elements C, N, and O were mainly detected in the survey spectra of all CTF-involved samples (Fig. S3). Si was exclusively observed in SiO₂@CTFs, being absent in alkaline-treated samples, which directly demonstrates the successful removal of the SiO₂ templates. Correspondingly, Na was found in the H-CTF-Na sample, confirming the introduction of Na during the NaOH hydrothermal process (Fig. 2d). In Fig. 2f, the C 1s spectrum fits three distinct peaks centered at 284.6, 286.8, and 288.2 eV, which were assigned to adventitious carbon C–C sp²-hybridized bonds, sp²-hybridized carbon (N–C=N), and C=O, respectively [55]. The N 1s spectrum (Fig. 2e) was deconvoluted into two peaks centered at 398.7 and 399.8, which were assigned to the sp²-hybridized nitrogen in aromatic triazine rings (C–N=C) and uncondensed nitrile groups. Noticeably, in the C 1s and N 1s spectra of the treated samples (CTF-Na and H-CTF-Na), the peaks associated with sp²-hybridized C and N shifted slightly to higher binding energy ranges compared with those of the pure CTFs, indicating the migration of electron clouds induced by Na doping. The observed chemical shifts, coupled with XRD analysis, demonstrate the successful synthesis of Na-doped CTFs.

3.2. Efficient degradation of CBZ by solar-driven PMS activation

With the increasing discharge of pharmaceuticals and personal care products (PPCPs) into the environment, water contamination with PPCPs is becoming a severe public health problem [56]. Here, the photocatalytic activities of various catalysts toward the degradation of a typical pharmaceutical, CBZ, in water under different conditions were

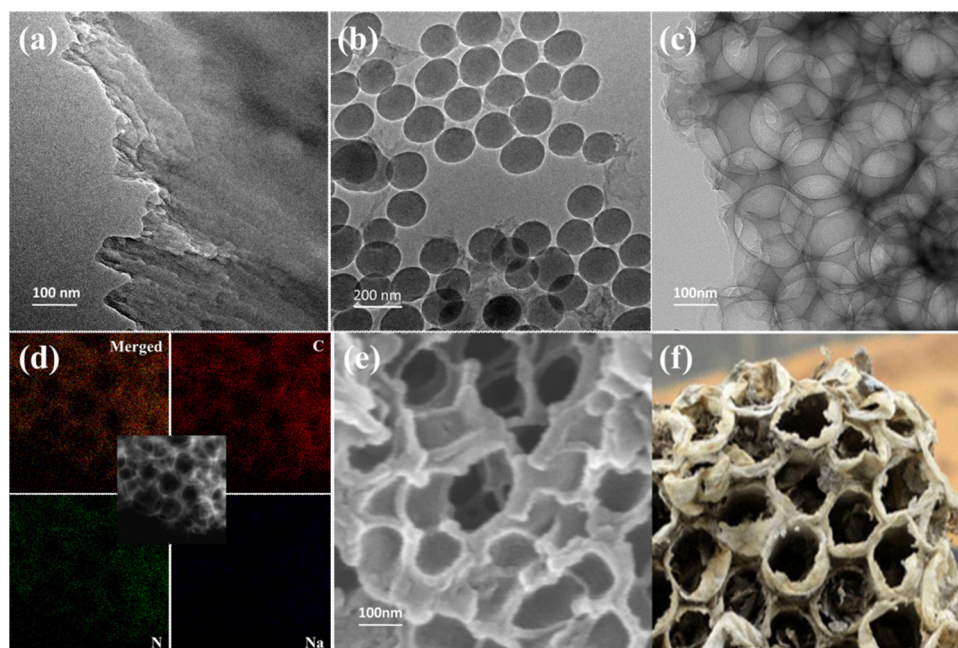


Fig. 1. TEM images of pristine CTFs (a), SiO₂@CTFs (b), and H-CTFs-Na (c); EDX elemental mapping and STEM image of H-CTFs-Na (d); and SEM image of H-CTFs-Na (e); photograph of the actual honeycomb (f).

investigated, and the results are shown in Fig. 3a. Without catalysts, PMS could not be activated well under visible-light irradiation to degrade CBZ. For all catalysts (CTFs, CTF-Na, and H-CTF-Na), photocatalytic PMS activation (catalyst/vis/PMS) was found to be much more efficient than photocatalytic oxidation (catalyst/vis) in degrading CBZ. These results suggested that the introduction of PMS into the photocatalytic systems could either decompose to generate highly reactive species or facilitate the separation of charge carriers by rapidly capturing photogenerated electrons. Impressively, the catalytic performance of alkaline hydrothermal-treated catalysts such as CTF-Na and H-CTF-Na in removing CBZ was superior to that of their counterparts (CTFs and SiO₂@CTFs), regardless of the presence of PMS. This finding confirmed the function of alkaline treatment in enhancing the photocatalytic activities of as-prepared materials. The H-CTF-Na/vis/PMS catalyst proved to be the most effective system for CBZ removal, and ~96.8% of the initial CBZ amount was degraded within 100 min. For comparison, only 46.6% and 29.8% CBZ removal could be reached for a solid SiO₂@CTFs catalyst without a hollow nanostructure and common g-C₃N₄ under the same conditions, respectively, far lower than that achieved by the H-CTF-Na catalyst. In a control experiment, H-CTF-Na/PMS in the absence of any light irradiation also exhibited inferior CBZ removal efficiency (24.6% within 100 min), indicating that the performance of the catalyst in simple catalytic oxidation was very poor. Based on the pseudo-first-order kinetics of CBZ degradation by various oxidation methods, CBZ removal rate constants were calculated and are displayed in Fig. 3b. H-CTF-Na/vis/PMS showed the highest k value of 0.0302 min⁻¹, which was five and eight times higher than that of the pristine CTFs catalyst system (CTFs/vis/PMS) and that of the photodecomposition system without PMS (H-CTF-Na/vis), respectively.

To explore the oxidative features of the H-CTF-Na/vis/PMS system, the effects of operating parameters (including H-CTF-Na dosage, CBZ concentration, PMS concentration, and solution pH) on CBZ degradation were evaluated systematically. The CBZ degradation was enhanced when increased the dosage of both H-CTF-Na and PMS to some extents, while its efficiency decreased with increasing CBZ concentration (discussions are detailed in Fig. S4). Moreover, the H-CTF-Na/vis/PMS system showed effective photocatalytic activity toward CBZ degradation over a broad initial pH range. The mineralization degree of CBZ in the H-CTF-Na/vis/PMS system expressed as total organic carbon (TOC)

removal (Fig. S5) reached 40.7%, which is higher than or comparable to the values reported in similar studies [57]. Conversely, only a 15.1% mineralization degree of CBZ was achieved in the H-CTF-Na/vis system without PMS due to the lack of reactive species, demonstrating the critical role of PMS in oxidation systems.

3.3. Photoelectrochemical results and density functional theory calculations

To determine the reasons for the differences between the various catalyst systems, the photoelectrochemical properties of various samples were first examined. The UV–vis diffuse reflectance spectra (Fig. 4a) show that the absorption edge of the NaOH-treated catalysts (CTF-Na and H-CTF-Na) exhibit an obvious redshift compared with the spectra of the SiO₂@CTFs and CTFs due to the Na doping confirmed previously. Interestingly, the absorption intensity of H-CTF-Na under visible light is higher than that of the other samples. This discrepancy might be attributed to the H-CTF-Na catalyst's 3D honeycomb nanostructure, as the unique hierarchical structure endows the catalyst with more efficient light harvesting owing to the multireflection within the interconnected hollow framework. The Tauc plots in Fig. 4b show that narrowed intrinsic band-gap energy values were obtained for CTF-Na (2.89 eV) and H-CTF-Na (2.88 eV) compared with the values obtained for the CTF (3.01 eV) and SiO₂@CTF (3.0 eV) samples.

Density functional theory (DFT) calculations were further carried out to gain an in-depth understanding of the electronic properties of pristine and Na-doped CTFs. The optimized structures of pure CTFs and CTF-Na with three possible positions of the Na atom are shown in Fig. 4e. With regard to all relaxed configurations, Na atoms are located out of plane (Fig. S6) due to the somewhat large radius (1.86 Å) and thus exert a certain influence on the crystal structure, as confirmed by the XRD results. The density of states (DOS) of each system was calculated and is depicted in Fig. 4e. The values of E_g (band gap between the conduction band (CB) minimum and the valence band (VB) maximum) for CTFs, CTF-Na1, CTF-Na2, and CTF-Na3 are 2.69 eV, 1.50 eV, 1.55 eV, and 1.85 eV, respectively. Although they are smaller than the experimental values, as DFT calculations consistently underestimate the energy gaps, the results prove that Na doping indeed narrows the band gaps. The Na atom barely participates in the formation of the VB top, but it can affect the band gap and band edge position because of its

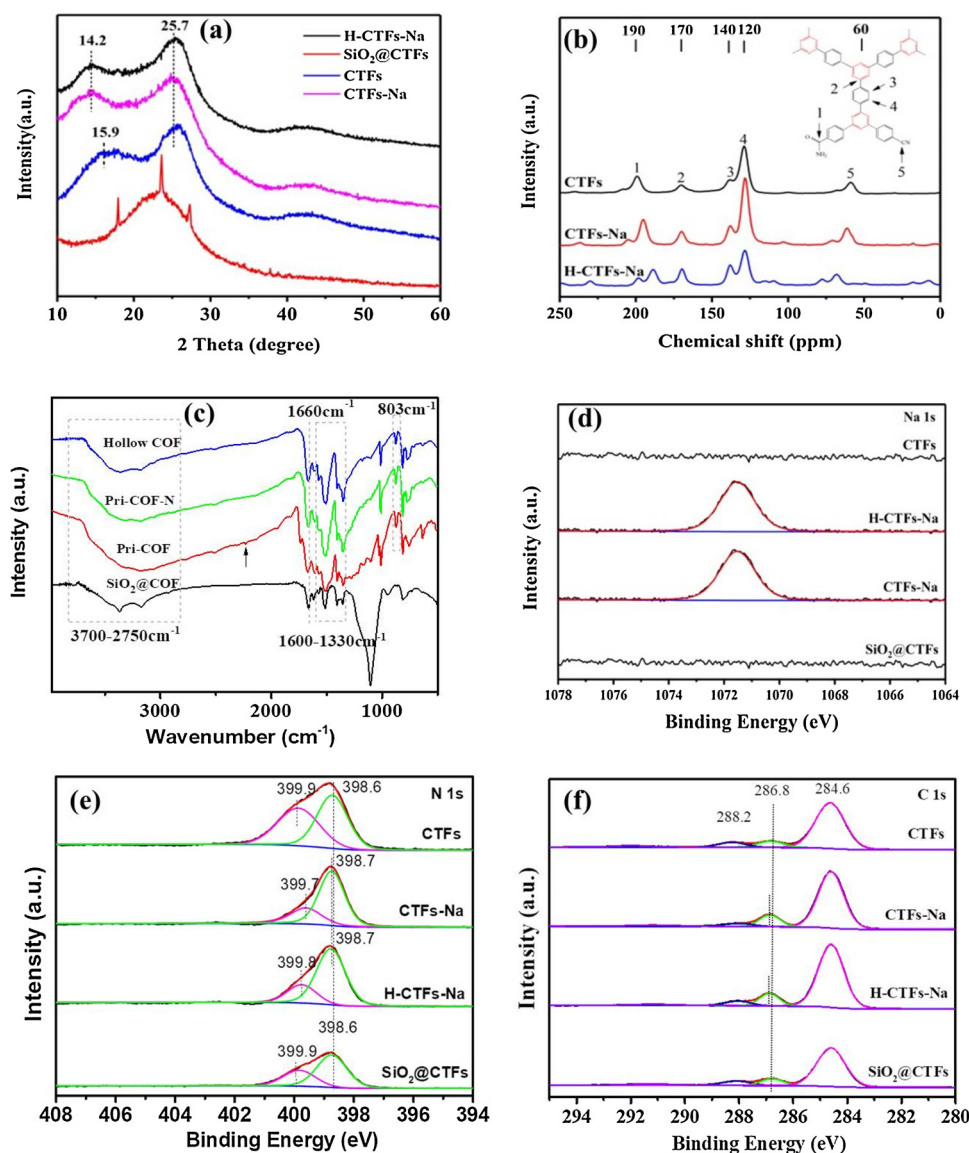


Fig. 2. Powder X-ray diffraction spectra (a), solid-state ^{13}C NMR spectra (b), and FT-IR spectra of different samples. XPS spectra of core-level Na 1s (d), N 1s (e), and C 1s (f).

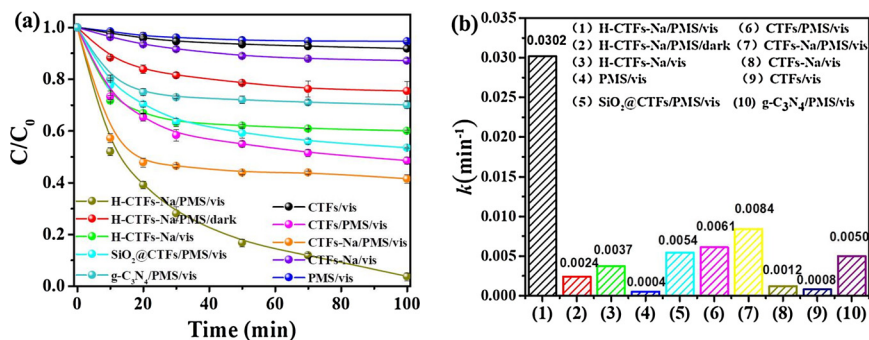


Fig. 3. Removal of CBZ in various systems (a) and the corresponding pseudo-first-order constants (b). Reaction conditions: [PMS] = 1.3 mM, [CBZ]₀ = 5 mg L⁻¹, [Cat.] = 0.40 g L⁻¹, initial pH = 7, and [Temp] = 25 °C.

ability to donate electrons to CTFs. This effect was reflected by the perturbed charge distribution calculated by DFT (Fig. S7) and the lowered VB edge estimated by VB-XPS after the introduction of the Na atom (Fig. S8). Therefore, the intercalated Na atoms into the CTFs interlayer are expected to form a bridge for the transfer and separation of

charge carriers.

To evaluate the transfer efficiency of photocarriers (photoexcited electrons and holes) in the catalysts, photocurrent generation (Fig. 4c) and electrochemical impedance spectroscopy (EIS, Fig. 4d) were performed. Compared with pristine CTFs, CTF-Na presented an improved

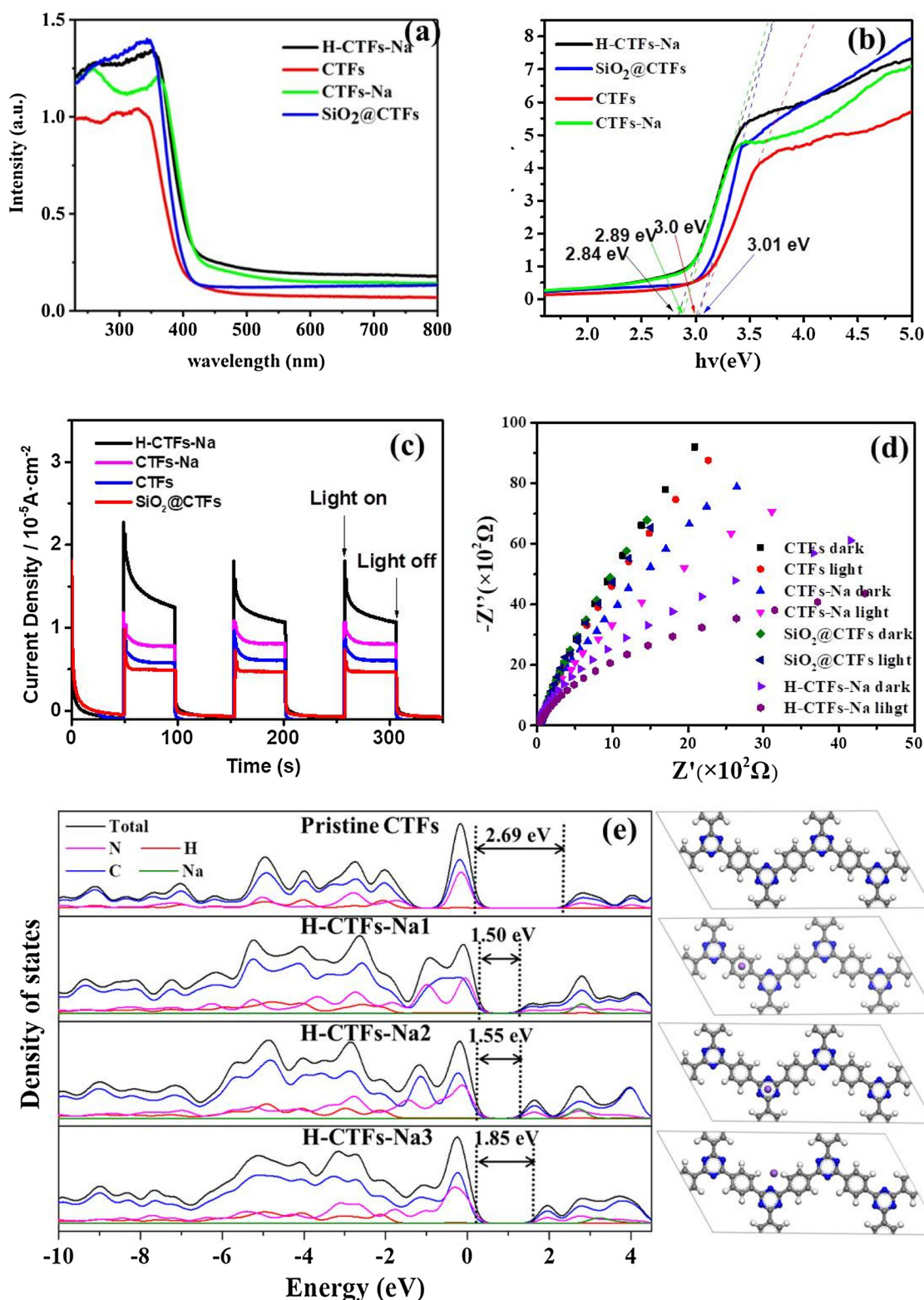


Fig. 4. Diffuse reflectance UV-vis spectra (a), Tauc plots (b), transient photocurrent response (at 1.2 V bias vs. Ag/AgCl) (c), and EIS Nyquist plot in the presence or absence of visible light irradiation (d) for various materials; Calculated density of states (DOS) and optimized geometries of pristine CTFs and H-CTFs-Na with different Na positions (e).

transient photocurrent, and further enhanced photocurrent was achieved for H-CTF-Na. This finding confirms that the generation and mobility of photoexcited charges under visible-light irradiation could be facilitated by Na doping and the 3D honeycomb nanostructures. Moreover, the arc radii of H-CTF-Na in EIS Nyquist plots are smaller

than those of all the other catalysts, indicating that the sample exhibits the lowest resistance for charge transfer in the framework, benefiting from photogenerated electron-hole separation and the reduction in photocarrier recombination efficiency. Briefly, for the H-CTF-Na photocatalyst, the experimental and theoretical results demonstrate that its

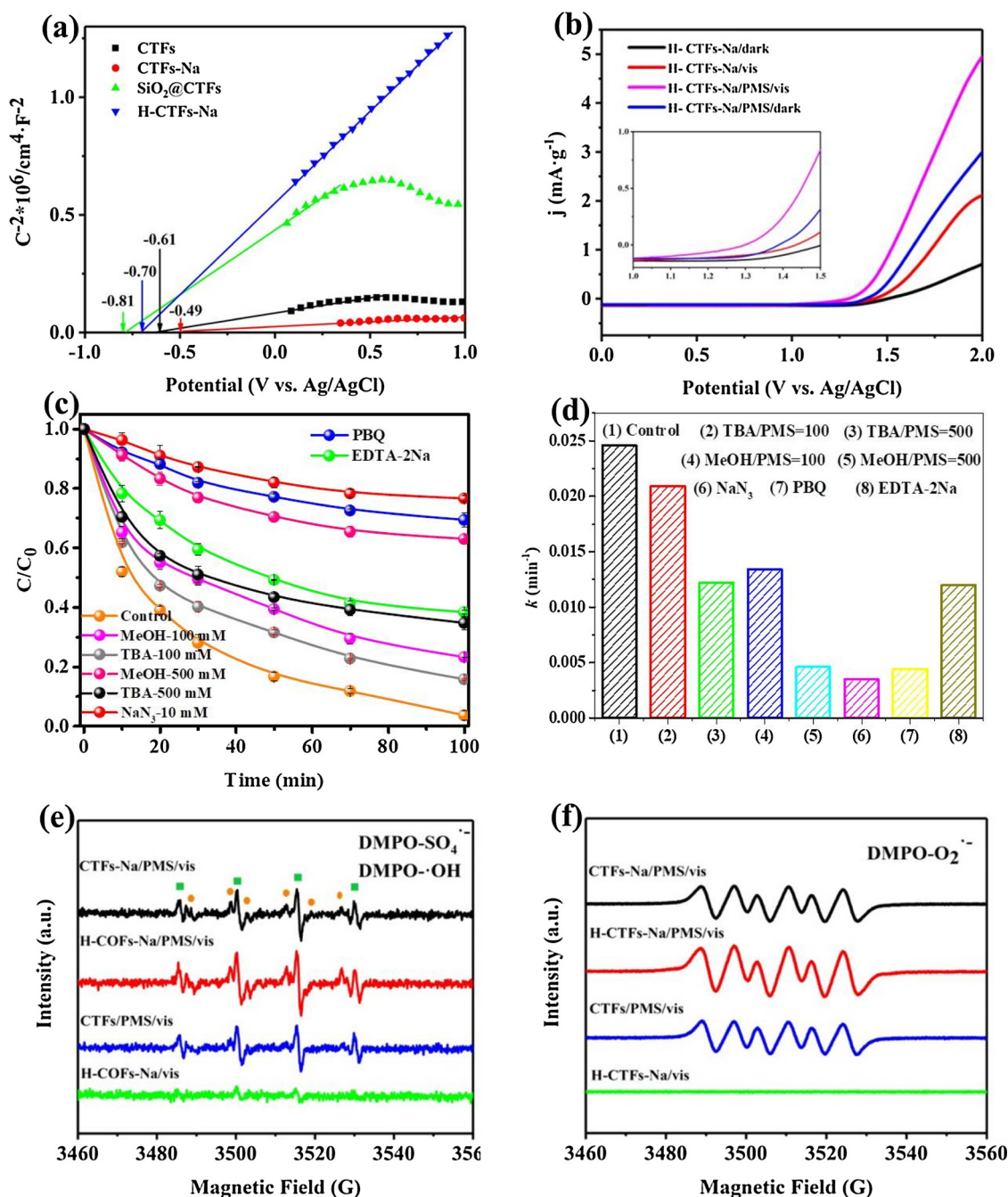


Fig. 5. (a) M-S plots measured at a frequency of 1000 Hz in the dark (conditions: 0.1 M Na_2SO_4 , pH = 6.8); (b) linear scanning voltammetry (LSV) curves in the presence or absence of 1.3 mM PMS; (c) inhibiting effects of quenching agents on CBZ degradation in H-CTFs-Na/vis/PMS system, and (d) the corresponding pseudo-first-order constants; EPR spectra of different systems using DMPO as the spin-trapping agent in water (e) and in ethanol (f).

unique composition and nanocellular framework are more favorable for photocatalysis.

3.4. Mechanistic insights into solar-driven PMS activation

To better understand the mechanism for the accelerated photocatalytic degradation of CBZ in the H-CTF-Na/vis/PMS system, the band structure of H-CTF-Na with respect to the redox ability of photoinduced charge carriers was evaluated. Typical Mott-Schottky plots of various catalysts measured at a frequency of 100 Hz in the dark are shown in Fig. 5a, which reveals an n-type semiconductor feature for all CTF-based materials for the positive slopes of all plots. The flat potentials of the CTF, CTF-Na, $\text{SiO}_2@\text{CTFs}$, and H-CTF-Na samples were

extrapolated to be -0.61, -0.49, -0.81, and -0.70 V versus Ag/AgCl, equivalent to -0.41, -0.29, -0.61, and -0.50 V versus normal hydrogen electrode (NHE). It has been reported that the flat-band potential of n-type semiconductors is usually 0–0.1 V higher than the conduction-band potential [58]. Therefore, the corresponding schematic diagrams of the energy band structure versus NHE for various samples were drawn (see Fig. S9). When illuminated with photons of energy exceeding the band gap (2.88 eV), photoinduced electrons and holes are formed and migrate, if they escape recombination, to the H-CTF-Na polymer surface to produce ROS for oxidizing CBZ. Since the potential energy of VB of H-CTF-Na was more negative than the redox potential of $\text{SO}_4^{\cdot-}/\text{SO}_4^{2-}$ (2.5–3.1 V vs NHE), the photogenerated electron could be trapped by PMS to create $\text{SO}_4^{\cdot-}$. The role of PMS in the

photocatalytic process was confirmed by linear scanning voltammetry (LSV) measurements of the H-CTF-Na current with and without PMS. As shown in Fig. 5b, the current of H-CTF-Na under visible-light irradiation was higher than in the dark, and it increased remarkably in the presence of PMS regardless of whether light irradiation was implemented. This finding is reasonable because PMS can serve as an electron acceptor to favor the transmission efficiency of photoinduced electrons and thus enhance the current generated in systems.

To ascertain the primary reactive radicals responsible for CBZ removal, various quenching tests and comparative electron paramagnetic resonance (EPR) studies were carried out. The addition of *tert*-butyl alcohol (TBA, 100 mM), methanol (MeOH, 100 mM), and sodium azide (NaN_3 , 10 mM) led to inhibition rates of ~15%, ~20%, and ~74%, respectively (Fig. 5c and d). Although NaN_3 is usually used as singlet oxygen ($^1\text{O}_2$) scavenger, it is also efficient quencher for $\cdot\text{OH}$ and $\text{SO}_4^{\cdot-}$. According to the rate constants of $^1\text{O}_2$, $\cdot\text{OH}$, and $\text{SO}_4^{\cdot-}$ quenched by MeOH and NaN_3 (Table S2), we then calculated their scavenging capacities based on kc value (where k is the rate constant and c is the concentration of quencher). For NaN_3 at 10 mM, the scavenging capacities for $^1\text{O}_2$, $\cdot\text{OH}$, and $\text{SO}_4^{\cdot-}$ are 1.0×10^7 , 1.2×10^8 , and $2.52 \times 10^7 \text{ s}^{-1}$, respectively. Although the scavenging capacities for $^1\text{O}_2$ is higher than that of 100 mM MeOH ($3.0 \times 10^2 \text{ s}^{-1}$), these values for $\cdot\text{OH}$ and $\text{SO}_4^{\cdot-}$ also beat those of MeOH (9.7×10^7 and $2.5 \times 10^6 \text{ s}^{-1}$, respectively), which therefore implied that the relatively stronger kinetic retardation of NaN_3 cannot be unquestionably attributed to $^1\text{O}_2$ scavenging. Subsequently, the concentration of MeOH was increased to 500 mM so that the scavenging capacities for $\cdot\text{OH}$ and $\text{SO}_4^{\cdot-}$ (4.85×10^8 and $1.25 \times 10^7 \text{ s}^{-1}$, respectively) are comparable to 10 mM NaN_3 , and one can found the inhibition effects for CBZ removal increased accordingly (Fig. 5c). This indicates that $\cdot\text{OH}$ and $\text{SO}_4^{\cdot-}$ were the dominant oxidative species in the degradation process. EPR results using 5,5-dimethyl-1-pyrroline-*N*-oxide (DMPO) as spin-trapping reagents also shows that the DMPO- $\cdot\text{OH}$ and DMPO- $\text{SO}_4^{\cdot-}$ signals could be detected in CTFs/vis/PMS, CTF-Na/vis/PMS, and H-CTF-Na/vis/PMS systems. To further identify the possible role of $^1\text{O}_2$ (since the inhibition effect of 10 mM NaN_3 is still stronger than 500 mM MeOH), we exchanged the solvent of the reaction system from water to D_2O which is reported to be an enhancer for singlet oxygenation [59]. Negligible acceleration in CBZ removal can be found (Fig. S10a), demonstrating that $^1\text{O}_2$ actually played a minor role (if present) on CBZ degradation in the H-CTF-Na/PMS/vis system. The superior retardation of NaN_3 to MeOH may be due to the depletion of PMS by excess NaN_3 through direct reaction [59,60], as confirmed by the result in Fig. S10b.

In addition, the CBZ degradation was also retarded by addition of EDTA-2Na as holes scavenger, verifying the possible role of photo-generated holes during the oxidation process. The oxidation potential of photogenerated h^+ in H-CTF-Na photocatalyst could be estimated as +2.23 V vs. NHE, higher than the redox potential of CBZ (1.31 V vs. NHE) but lower than that of $\cdot\text{OH}/\text{HO}^-$ (+2.80 V vs. NHE) [61], which suggests that the direct h^+ oxidation of CBZ is energetically possible while the possibility of h^+ directly oxidize H_2O to yield $\cdot\text{OH}$ could be ruled out. To further ascertain the former, Ag(I) instead of PMS as electron acceptor was added into the H-CTF-Na/vis photooxidation system. The results in Fig. S11 show that the photooxidation of CBZ was indeed significantly enhanced and thus affirm the crucial role of photo-generated h^+ during the oxidation.

Therefore, it is likely that PMS markedly accelerates the photocatalytic oxidation of CBZ in two ways: by generating $\text{SO}_4^{\cdot-}$ and $\cdot\text{OH}$ through its reductive conversion as well as the enhancing the charge separation by capturing CB^- . As PMS (1.82 V vs NHE) is much more oxidative than O_2 (1.23 V vs NHE), CB^- are thermodynamically more easily captured by PMS, which can then be activated to produce radicals ($\text{HSO}_5^- + e^- \rightarrow \text{SO}_4^{\cdot-} + \text{HO}^-$; $\text{SO}_4^{\cdot-} + \text{H}_2\text{O} \rightarrow \cdot\text{OH} + \text{SO}_4^{2-} + \text{H}^+$). When nitrogen was purged into the solution, the CBZ degradation can seldom be affected (Fig. S12), which further excludes the role of dissolved oxygen as ROS precursor. The EPR appearance of the DMPO-

$\text{O}_2^{\cdot-}$ adducts (Fig. 5e), together with the quenching result of *p*-benzoquinone (*p*-BQ), is clear evidence for $\text{O}_2^{\cdot-}$ production ($2\text{HSO}_5^- + e^- \rightarrow 2\text{HSO}_4^- + \text{O}_2^{\cdot-}$) but does not prove its direct participation in degradation of CBZ in this system. Considering that the redox potential of $\text{O}_2^{\cdot-}$ (0.91 V) is much lower than those of $\cdot\text{OH}$ (1.9–2.7 V) and $\text{SO}_4^{\cdot-}$ (2.5–3.1 V) [62], it may be not very reactive with organic compounds in aqueous solution [60]. Therefore, it would be reasonable to regard $\text{O}_2^{\cdot-}$ as intermediate to form other reactive species, such as $\cdot\text{OH}$ ($\text{HSO}_5^- + \text{O}_2^{\cdot-} \rightarrow \cdot\text{OH} + \text{SO}_4^{2-} + \text{O}_2$), $\text{SO}_4^{\cdot-}$ ($\text{HSO}_5^- + \text{O}_2^{\cdot-} \rightarrow \text{OH}^- + \text{SO}_4^{\cdot-} + \text{O}_2$), and $^1\text{O}_2$ ($2\text{O}_2^{\cdot-} + 2\text{H}_2\text{O} \rightarrow ^1\text{O}_2 + \text{H}_2\text{O}_2 + 2\text{OH}^-$) [63]. Finally, the triplet TEMPO signals in EPR spectra were also observed (Fig. S13), we thus cannot completely rule out the existence of $^1\text{O}_2$ in H-CTF-Na/PMS/vis system, although it contributes little to CBZ removal. Above all, it is proposed that the H-CTF-Na/vis/PMS oxidation system involves a synergistic effect of photooxidation and PMS chemical activation, in which h^+ , $\cdot\text{OH}$, and $\text{SO}_4^{\cdot-}$ are the main reactive species responsible for CBZ degradation.

3.5. Versatility and reusability of catalyst

To investigate the versatility of H-CTF-Na/PMS/vis system, several phenols and dyes (those were commonly selected as targets in other similar studies) were also oxidized by H-CTF-Na/PMS/vis system. As shown in Fig. 6a, all of them (i.e. bisphenol A, phenol, 4-chlorophenol, Acid Orange 7, and Rhodamine B, 100 μM) can be fast removed even under a relatively lower addition of H-CTF-Na (0.1 g L^{-1}) and PMS (0.65 mM), which demonstrates the good versatility of H-CTF-Na/PMS/vis system for organic pollutant treatment. When compared with other similar studies (Table S3), the catalytic efficiency of the as-prepared H-CTF-Na is absolutely superior to other $g\text{-C}_3\text{N}_4$ -based polymeric photocatalysts, and even comparable or higher than those of most inorganic photocatalysts. The utilization efficiency of PMS for the oxidation of organics was examined by calculating the ratio of the oxidized organics molar concentration ($\Delta[\text{Organics}]$) to the consumed PMS molar concentration ($\Delta[\text{PMS}]$) (Fig. S14). From Fig. 6b one can see that the utilization efficiency of PMS for CBZ oxidation is rather low (only with 5.7%), but it can be reach to ~27% for all phenols and dyes applied, implying the relatively highly persistent nature of CBZ [26]. The degradation of CBZ in various water matrices including treated effluent water, surface water, and tap water were also investigated (Fig. S15). It was found that the degradation rate of CBZ in tap water is comparable to that in DI water, but somewhat decreases in treated effluent water and surface water, which might be contributed to the competing side reactions of radicals with the background organic species in the latter two water matrices [64–66].

Two issues of critical concern regarding the practical application of catalysts are reusability and stability, which were examined by performing the same photocatalytic experiment continuously over multiple cycles. As shown in Fig. 6c, despite a slight decline, over 82% removal efficiency of CBZ could be achieved within 100 min even after five successive rounds. No obvious changes were observed in either the crystallinity or elemental composition of H-CTF-Na after photocatalytic degradation, which was confirmed by XRD and XPS survey characterizations (Fig. S16a, S16b). The changes in XPS individual analysis of C (Fig. S16c), N (Fig. S16d), and Na (Fig. S16e) were negligible, but the intensity of O increased to some extent (Fig. 16f). This may be ascribed to the minor surface adsorption of oxidized intermediate products of CBZ decomposition, which could also be evidenced by the FTIR results where the weak C–N (2243 cm^{-1}) and C=O (1830 cm^{-1}) stretching vibrations emerged (Fig. S17a). However, this insignificant surface adsorption seems cannot influence the optical band properties of H-CTF-Na, as proved by the almost unchanged UV–vis diffuse reflectance spectra (Fig. S17b). Furthermore, the structure of the H-CTF-Na catalyst was well retained, and the morphology did not change after use according to TEM measurements (Fig. S16c). Also we determined the possible leaching of Na ion by ICP-OES analysis and found almost no

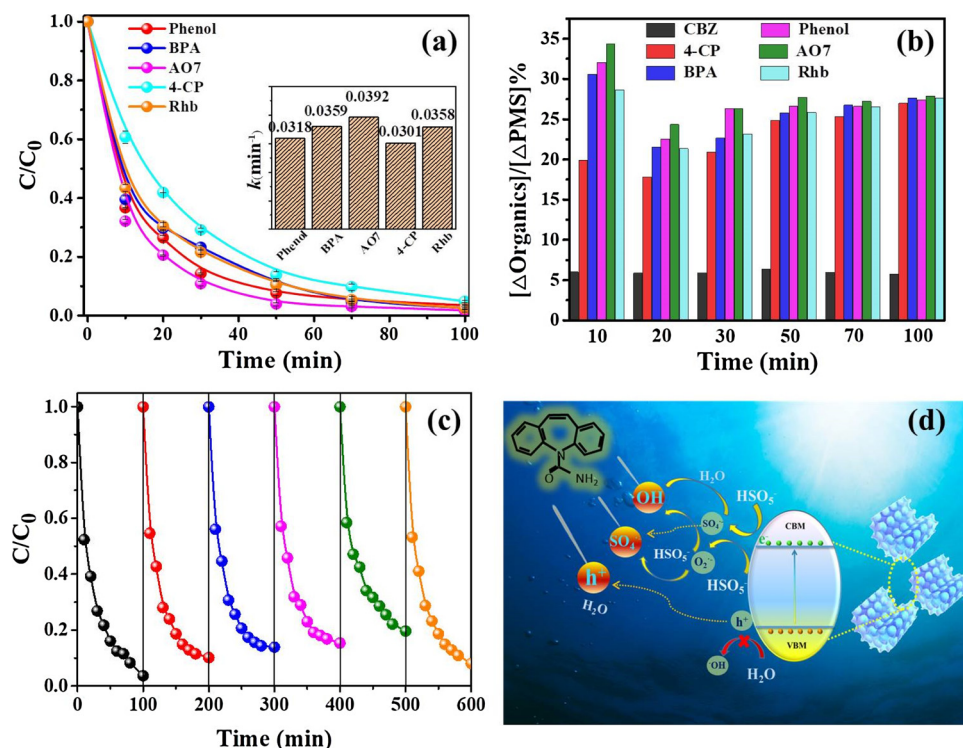


Fig. 6. (a) Degradation of different organic pollutants by H-CTF-Na/PMS/vis system (Conditions: [Cat.] = 0.1 g L⁻¹, [PMS] = 0.65 mM, initial pH = 7, Temp. = 25 °C, bisphenol A = phenol = 4-chlorophenol = Acid Orange 7 = Rhodamine B = 100 μM); (b) the utilization efficiency of PMS for the oxidation of various organics; (c) reusability of H-CTFs-Na photocatalyst; and (d) proposed catalytic degradation mechanism of H-CTF-Na/vis/PMS system.

leaching was detected (data were not shown).

Therefore, the reason for the decrease in removal efficiency of CBZ upon reuse is most probably the catalyst loss during recycling. The catalyst loss was found to be 1.25%, 6.0%, 12.75%, and 18.0% of initial dosage in the second, third, fourth, and fifth run, respectively. And the catalytic activity was significantly recovered when additional fresh H-CTF-Na catalyst was supplemented for the loss during recycling (Fig. 6c). The robust stability and reusability therefore endow the H-CTF-Na catalyst with great promise for water decontamination.

In light of the foregoing discussion, a reasonable mechanism for the enhanced photocatalytic oxidation of CBZ in the H-CTF-Na/vis/PMS system was established (Fig. 6d). It is well known that three key steps are commonly involved in heterogeneous photocatalysis: I) light harvesting for photoexcitation of charge carriers, II) charges escaping recombination and transferring to the catalyst surface, and III) surface redox reactions; these steps are greatly affected by the inherent properties of the photocatalysts, such as their band gap, composition and morphology. Herein, the characteristics of the as-prepared H-CTF-Na meet the requirement of enhanced photocatalytic performance. More specifically, Na doping into the CTFs narrows the band gap by elevating the band edges and extends the visible-light absorption boundary. The 3D hierarchical honeycomb scaffold allows for multiple reflections and scattering of incident light within the interiors of cavities and shortens the transport distance of charges to the surface, thus enhancing light harvesting and reducing the recombination probability of the photoexcited carriers. Therefore, H-CTF-Na can gain more solar energy to produce more photogenerated charges under visible-light irradiation compared to pristine CTFs. After the introduction of PMS, the separation of charge carriers is further accelerated due to the rapid capture of photogenerated electrons, while PMS itself decomposes to various reactive species through a series of chain reactions, which introduces a synergistic effect between photooxidation (mainly h^+) and PMS chemical activation (mainly $\cdot OH$ and $SO_4^{\cdot -}$) for CBZ degradation. Additionally, features such as abundant accessible active sites, good permeability, and high hydrophilicity exhibited by the H-CTF-Na photocatalyst also favor the photocatalysis reaction. As a result, the formed reactive species decompose the CBZ molecules rapidly around

the catalytic center.

4. Conclusion

In conclusion, H-CTF-Na polymer photocatalysts with 3D hierarchical honeycomb nanoarchitectures and Na doping were facilely synthesized for efficient solar-driven water purification. We found that a 3D nanocellular design combined with simultaneous Na doping could affect the electronic structure and improve light harvesting, which are favorable for the formation of more photogenerated charges under visible-light irradiation, causing the photocatalytic performance of H-CTF-Na to be superior to that of pristine CTFs and g-C₃N₄ for CBZ photodegradation. Moreover, the CBZ degradation efficiency achieved by the H-CTF-Na/vis/PMS system far exceeds that achieved by photo-oxidation (H-CTF-Na/vis) or PMS activation (H-CTF-Na/PMS) alone by factors of 8 and 12. The reason is that PMS can rapidly capture CBZ- e^- to facilitate the separation of charge carriers and produce abundant reactive species, thereby giving rise to the collaboration between photo-oxidation (h^+) and PMS-activation ($\cdot OH$, $SO_4^{\cdot -}$) processes for CBZ oxidation. Furthermore, H-CTF-Na-based system exhibited excellent versatility in degrading other organics and good reusability in terms of five high-efficiency recycled uses. The results obtained in the present work may represent a significant advance in developing semi-conducting-based polymer photocatalysts for solar-driven AOPs, which opens a green and facile method for water decontamination.

Declaration of Competing Interest

There are no conflicts to declare.

Acknowledgements

We thank the National Natural Science Foundation of China (21876156 and 21607130), the Zhejiang Provincial Natural Science Foundation of China (LZ18B070001 and LGF18E080017), the Opening Project of State Key Laboratory of Environmental Chemistry and Ecotoxicology (KF2016-29), and the Program for Changjiang Scholars

and Innovative Research Team in University (IRT13096) for financial support.

Appendix A. Supplementary data

Supplementary material related to this article can be found, in the online version, at doi:<https://doi.org/10.1016/j.apcatb.2019.117915>.

References

- [1] C.A. Martinez-Huitle, M.A. Rodrigo, I. Sires, O. Scialdone, Single and coupled electrochemical processes and reactors for the abatement of organic water pollutants: a critical review, *Chem. Rev.* 115 (24) (2015) 13362–13407.
- [2] Y. Xu, T.J. Liu, Y. Zhang, F. Ge, R.M. Steel, L.Y. Sun, Advances in technologies for pharmaceuticals and personal care products removal, *J. Mater. Chem. A* 5 (24) (2017) 12001–12014.
- [3] X.G. Duan, H.Q. Sun, S.B. Wang, Metal-free carbocatalysis in advanced oxidation reactions, *Accounts Chem. Res.* 51 (3) (2018) 678–687.
- [4] T. Zeng, M.D. Yu, H.Y. Zhang, Z.Q. He, J.M. Chen, S. Song, Fe/Fe₃C@N-doped porous carbon hybrids derived from nano-scale MOFs: robust and enhanced heterogeneous catalyst for peroxymonosulfate activation, *Catal. Sci. Technol.* 7 (2) (2017) 396–404.
- [5] Y. Zhou, J. Jiang, Y. Gao, J. Ma, S.Y. Pang, J. Li, X.T. Lu, L.P. Yuan, Activation of peroxymonosulfate by Benzoquinone: a novel nonradical oxidation process, *Environ. Sci. Technol.* 49 (21) (2015) 12941–12950.
- [6] T. Zeng, X.L. Zhang, S.H. Wang, H.Y. Niu, Y.Q. Cai, Spatial confinement of a Co₃O₄ catalyst in hollow metal-organic frameworks as a nanoreactor for improved degradation of organic pollutants, *Environ. Sci. Technol.* 49 (4) (2015) 2350–2357.
- [7] P.D. Hu, H.R. Su, Z.Y. Chen, C.Y. Yu, Q.L. Li, B.X. Zhou, P.J.J. Alvarez, M.C. Long, Selective degradation of organic pollutants using an efficient metal-free catalyst derived from carbonized polypyrrole via peroxymonosulfate activation, *Environ. Sci. Technol.* 51 (19) (2017) 11288–11296.
- [8] C.Z. Cui, L. Jin, L. Jiang, Q. Han, K.F. Lin, S.G. Lu, D. Zhang, G.M. Cao, Removal of trace level amounts of twelve sulfonamides from drinking water by UV-activated peroxymonosulfate, *Sci. Total Environ.* 572 (2016) 244–251.
- [9] S. Chakma, S. Praneeth, V.S. Moholkar, Mechanistic investigations in sono-hybrid (ultrasound/Fe²⁺/UV) techniques of persulfate activation for degradation of Azorubine, *Ultrason. Sonochem.* 38 (2017) 652–663.
- [10] H.D. Xu, D. Wang, J. Ma, T. Zhang, X.H. Lu, Z.Q. Chen, A superior active and stable spinel sulfide for catalytic peroxymonosulfate oxidation of bisphenol S, *Appl. Catal. B Environ.* 238 (2018) 557–567.
- [11] X.G. Duan, C. Su, J. Miao, Y.J. Zhong, Z.P. Shao, S.B. Wang, H.Q. Sun, Insights into perovskite-catalyzed peroxymonosulfate activation: maneuverable cobalt sites for promoted evolution of sulfate radicals, *Appl. Catal. B Environ.* 220 (2018) 626–634.
- [12] T. Zeng, S.Q. Li, J.A. Hua, Z.Q. He, X.L. Zhang, H.R. Feng, S. Song, Synergistically enhancing Fenton-like degradation of organics by in situ transformation from Fe₃O₄ microspheres to mesoporous Fe, N-dual doped carbon, *Sci. Total Environ.* 645 (2018) 550–559.
- [13] Y. Gao, Y. Zhu, L. Lyu, Q. Zeng, X. Xing, C. Hu, Electronic structure modulation of graphitic carbon nitride by oxygen doping for enhanced catalytic degradation of organic pollutants through peroxymonosulfate activation, *Environ. Sci. Technol.* 52 (24) (2018) 14371–14380.
- [14] T.D. Minh, M.C. Ncibi, V. Srivastava, S.K. Thangaraj, J. Jänis, M. Sillanpää, Gingerbread ingredient-derived carbons-assembled CNT foam for the efficient peroxymonosulfate-mediated degradation of emerging pharmaceutical contaminants, *Appl. Catal. B Environ.* 244 (2019) 367–384.
- [15] N. Jaafarzadeh, F. Ghanbari, M. Ahmadi, M. Omidinasab, Efficient integrated processes for pulp and paper wastewater treatment and phytotoxicity reduction: permanganate, electro-Fenton and Co₃O₄/UV/peroxymonosulfate, *Chem. Eng. J.* 308 (2017) 142–150.
- [16] G. Wen, X.L. Deng, Q.Q. Wan, X.Q. Xu, T.L. Huang, Photoreactivation of fungal spores in water following UV disinfection and their control using UV-based advanced oxidation processes, *Water Res.* 148 (2019) 1–9.
- [17] G. Matafonova, V. Batoev, Recent advances in application of UV light-emitting diodes for degrading organic pollutants in water through advanced oxidation processes: a review, *Water Res.* 132 (2018) 177–189.
- [18] J. Deng, Y.J. Ge, C.Q. Tan, H.Y. Wang, Q.S. Li, S.Q. Zhou, K.J. Zhang, Degradation of ciprofloxacin using alpha-MnO₂ activated peroxymonosulfate process: effect of water constituents, degradation intermediates and toxicity evaluation, *Chem. Eng. J.* 330 (2017) 1390–1400.
- [19] P. Liang, C. Zhang, X.G. Duan, H.Q. Sun, S.M. Liu, M.O. Tade, S.B. Wang, An insight into metal organic framework derived N-doped graphene for the oxidative degradation of persistent contaminants: formation mechanism and generation of singlet oxygen from peroxymonosulfate, *Environ. Sci. Nano* 4 (2) (2017) 315–324.
- [20] S.S. Zhu, X.C. Huang, F. Ma, L. Wang, X.G. Duan, S.B. Wang, Catalytic removal of aqueous contaminants on N-Doped graphitic biochars: inherent roles of adsorption and nonradical mechanisms, *Environ. Sci. Technol.* 52 (15) (2018) 8649–8658.
- [21] N. Wang, W.J. Ma, Z.Q. Ren, Y.C. Du, P. Xu, X.J. Han, Prussian blue analogues derived porous nitrogen-doped carbon microspheres as high-performance metal-free peroxymonosulfate activators for non-radical-dominated degradation of organic pollutants, *J. Mater. Chem. A* 6 (3) (2018) 884–895.
- [22] R.S. Sprick, J.X. Jiang, B. Bonillo, S.J. Ren, T. Ratvijitvech, P. Guiglion, M.A. Zwijnenburg, D.J. Adams, A.I. Cooper, Tunable organic photocatalysts for visible-light-driven hydrogen evolution, *J. Am. Chem. Soc.* 137 (9) (2015) 3265–3270.
- [23] R.S. Sprick, B. Bonillo, R. Clowes, P. Guiglion, N.J. Brownbill, B.J. Slater, F. Blanc, M.A. Zwijnenburg, D.J. Adams, A.I. Cooper, Visible-Light-Driven Hydrogen Evolution Using Planarized Conjugated Polymer Photocatalysts (vol 55, pg 1792, 2016), *Angew. Chemie Int. Ed. English* 57 (10) (2018) 2520–2520.
- [24] X.Y. Wang, L.J. Chen, S.Y. Chong, M.A. Little, Y.Z. Wu, W.H. Zhu, R. Clowes, Y. Yan, M.A. Zwijnenburg, R.S. Sprick, A.I. Cooper, Sulfone-containing covalent organic frameworks for photocatalytic hydrogen evolution from water, *Nat. Chem.* 10 (12) (2018) 1180–1189.
- [25] S. Ghosh, N.A. Kouame, L. Ramos, S. Remita, A. Dazzi, A. Deniset-Besseau, P. Beauvier, F. Goubard, P.H. Aubert, H. Remita, Conducting polymer nanostructures for photocatalysis under visible light, *Nat. Mater.* 14 (5) (2015) 505–511.
- [26] H. Kim, H.Y. Yoo, S. Hong, S. Lee, S. Lee, B.S. Park, H. Park, C. Lee, J. Lee, Effects of inorganic oxidants on kinetics and mechanisms of WO₃-mediated photocatalytic degradation, *Appl. Catal. B Environ.* 162 (2015) 515–523.
- [27] Y.B. Wang, X. Zhao, D. Cao, Y. Wang, Y.F. Zhu, Peroxymonosulfate enhanced visible light photocatalytic degradation bisphenol A by single-atom dispersed Ag mesoporous g-C₃N₄ hybrid, *Appl. Catal. B Environ.* 211 (2017) 79–88.
- [28] Y.W. Gao, S.M. Li, Y.X. Li, L.Y. Yao, H. Zhang, Accelerated photocatalytic degradation of organic pollutant over metal-organic framework MIL-53(Fe) under visible LED light mediated by persulfate, *Appl. Catal. B Environ.* 202 (2017) 165–174.
- [29] S.F. An, G.H. Zhang, T.W. Wang, W.N. Zhan, K.Y. Li, C.S. Song, J.T. Miller, S. Miao, J.H. Wang, X.W. Guo, High-density ultra-small clusters and single-atom Fe sites embedded in graphitic carbon nitride (g-C₃N₄) for highly efficient catalytic advanced oxidation processes, *ACS Nano* 12 (9) (2018) 9441–9450.
- [30] H.H. Gao, H.C. Yang, J.Z. Xu, S.W. Zhang, J.X. Li, Strongly coupled g-C₃N₄ Nanosheets-Co₃O₄ quantum dots as 2D/0D heterostructure composite for peroxymonosulfate activation, *Small* 14 (31) (2018).
- [31] F. Wu, H.W. Huang, T.F. Xu, W.Y. Lu, N. Li, W.X. Chen, Visible-light-assisted peroxymonosulfate activation and mechanism for the degradation of pharmaceuticals over pyridyl-functionalized graphitic carbon nitride coordinated with iron phthalocyanine, *Appl. Catal. B Environ.* 218 (2017) 230–239.
- [32] Y. Gong, X. Zhao, H. Zhang, B. Yang, K. Xiao, T. Guo, J.J. Zhang, H.X. Shao, Y.B. Wang, G. Yu, MOF-derived nitrogen doped carbon modified g-C₃N₄ heterostructure composite with enhanced photocatalytic activity for bisphenol A degradation with peroxymonosulfate under visible light irradiation, *Appl. Catal. B Environ.* 233 (2018) 35–45.
- [33] W. Liu, Y. Li, F. Liu, W. Jiang, D. Zhang, J. Liang, Visible-light-driven photocatalytic degradation of diclofenac by carbon quantum dots modified porous g-C₃N₄: mechanisms, degradation pathway and DFT calculation, *Water Res.* 151 (2019) 8–19.
- [34] D. Masih, Y.Y. Ma, S. Rohani, Graphitic C₃N₄ based noble-metal-free photocatalyst systems: a review, *Appl. Catal. B Environ.* 206 (2017) 556–588.
- [35] W. Huang, B.C. Ma, H. Lu, R. Li, L. Wang, K. Landfester, K.A.I. Zhang, Visible-light-Promoted selective oxidation of alcohols using a covalent triazine framework, *ACS Catal.* 7 (8) (2017) 5438–5442.
- [36] A. Bhunia, S. Dey, M. Bous, C.Y. Zhang, W. von Rybinski, C. Janiak, High adsorptive properties of covalent triazine-based frameworks (CTFs) for surfactants from aqueous solution, *Chem. Commun.* 51 (3) (2015) 484–486.
- [37] Y.F. Zhao, K.X. Yao, B.Y. Teng, T. Zhang, Y. Han, A perfluorinated covalent triazine-based framework for highly selective and water-tolerant CO₂ capture, *Energy Environ. Sci.* 6 (12) (2013) 3684–3692.
- [38] S.J. He, B. Yin, H.Y. Niu, Y.Q. Cai, Targeted synthesis of visible-light-driven covalent organic framework photocatalyst via molecular design and precise construction, *Appl. Catal. B Environ.* 239 (2018) 147–153.
- [39] X. Jiang, P. Wang, J.J. Zhao, 2D covalent triazine framework: a new class of organic photocatalyst for water splitting, *J. Mater. Chem. A* 3 (15) (2015) 7750–7758.
- [40] P. Pachfule, A. Acharjya, J. Roeser, T. Langenhahn, M. Schwarze, R. Schomacker, A. Thomas, J. Schmidt, Diacetylene functionalized covalent organic framework (COF) for photocatalytic hydrogen generation, *J. Am. Chem. Soc.* 140 (4) (2018) 1423–1427.
- [41] Z.A. Lan, Y.X. Fang, Y.F. Zhang, X.C. Wang, Photocatalytic oxygen evolution from functional triazine-based polymers with tunable band structures, *Angew. Chem. Int. Ed.* 57 (2) (2018) 470–474.
- [42] W. Huang, Z.J. Wang, B.C. Ma, S. Ghasimi, D. Gehrig, F. Laquai, K. Landfester, K.A.I. Zhang, Hollow nanoporous covalent triazine frameworks via acid vapor-assisted solid phase synthesis for enhanced visible light photoactivity, *J. Mater. Chem. A* 4 (20) (2016) 7555–7559.
- [43] L.Y. Li, W. Fang, P. Zhang, J.H. Bi, Y.H. He, J.Y. Wang, W.Y. Su, Sulfur-doped covalent triazine-based frameworks for enhanced photocatalytic hydrogen evolution from water under visible light, *J. Mater. Chem. A* 4 (32) (2016) 12402–12406.
- [44] Z. Cheng, W. Fang, T.S. Zhao, S.Q. Fang, J.H. Bi, S.J. Liang, L.Y. Li, Y. Yu, L. Wu, Efficient visible-light-Driven photocatalytic hydrogen evolution on phosphorus-doped covalent triazine-based frameworks, *ACS Appl. Mater. Interfaces* 10 (48) (2018) 41415–41421.
- [45] S.E. Guo, H.Y. Zhang, Y. Chen, Z.H. Liu, B. Yu, Y.F. Zhao, Z.Z. Yang, B.X. Han, Z.M. Liu, Visible-Light-Driven Photoreduction of CO₂ to CH₄ over N,O,P-Containing Covalent Organic Polymer Submicrospheres, *ACS Catal.* 8 (5) (2018) 4576–4581.
- [46] S.Q. Song, C.H. Lu, X. Wu, S.J. Jiang, C.Z. Sun, Z.G. Le, Strong base g-C₃N₄ with perfect structure for photocatalytically eliminating formaldehyde under visible-light irradiation, *Appl. Catal. B Environ.* 227 (2018) 145–152.
- [47] S.W. Cao, Q. Huang, B.C. Zhu, J.G. Yu, Trace-level phosphorus and sodium co-doping of g-C₃N₄ for enhanced photocatalytic H₂ production, *J. Power Sources* 351 (2017) 151–159.
- [48] Y.C. Wei, J.Q. Jiao, Z. Zhao, W.J. Zhong, J.M. Li, J. Liu, G.Y. Jiang, A.J. Duan, 3D

- ordered macroporous TiO₂-supported Pt@CdS core-shell nanoparticles: design, synthesis and efficient photocatalytic conversion of CO₂ with water to methane, *J. Mater. Chem. A* 3 (20) (2015) 11074–11085.
- [49] J.H. Sun, J.S. Zhang, M.W. Zhang, M. Antonietti, X.Z. Fu, X.C. Wang, Bioinspired hollow semiconductor nanospheres as photosynthetic nanoparticles, *Nat. Commun.* 3 (2012).
- [50] C.C. Nguyen, N.N. Vu, T.O. Do, Recent advances in the development of sunlight-driven hollow structure photocatalysts and their applications, *J. Mater. Chem. A* 3 (36) (2015) 18345–18359.
- [51] T. Zeng, M.D. Yu, H.Y. Zhang, Z.G. He, X.L. Zhang, J.M. Chen, S. Song, In situ synthesis of cobalt ferrites-embedded hollow N-doped carbon as an outstanding catalyst for elimination of organic pollutants, *Sci. Total Environ.* 593 (2017) 286–296.
- [52] X.C. Wang, K. Maeda, A. Thomas, K. Takanabe, G. Xin, J.M. Carlsson, K. Domen, M. Antonietti, A metal-free polymeric photocatalyst for hydrogen production from water under visible light, *Nat. Mater.* 8 (1) (2009) 76–80.
- [53] F. Guo, J.L. Chen, M.W. Zhang, B.F. Gao, B.Z. Lin, Y.L. Chen, Deprotonation of g-C₃N₄ with Na ions for efficient nonsacrificial water splitting under visible light, *J. Mater. Chem. A* 4 (28) (2016) 10806–10809.
- [54] K. Schwinghammer, S. Hug, M.B. Mesch, J. Senker, B.V. Lotsch, Phenyl-triazine oligomers for light-driven hydrogen evolution, *Energy Environ. Sci.* 8 (11) (2015) 3345–3353.
- [55] S.H. Je, H.J. Kim, J. Kim, J.W. Choi, A. Coskun, Perfluoroaryl-elemental sulfur SNAr chemistry in covalent triazine frameworks with high sulfur contents for lithium-sulfur batteries, *Adv. Funct. Mater.* 27 (47) (2017).
- [56] A. Tello, B. Austin, T.C. Telfer, Selective pressure of antibiotic pollution on Bacteria of importance to public health, *Environ. Health Perspect.* 120 (8) (2012) 1100–1106.
- [57] S.Z. Wang, J.L. Wang, Degradation of carbamazepine by radiation-induced activation of peroxymonosulfate, *Chem. Eng. J.* 336 (2018) 595–601.
- [58] J.H. Huang, Q.C. Shang, Y.Y. Huang, F.M. Tang, Q. Zhang, Q.H. Liu, S. Jiang, F.C. Hu, W. Liu, Y. Luo, T. Yao, Y. Jiang, Z.Y. Pan, Z.H. Sun, S.Q. Wei, Oxyhydroxide nanosheets with highly efficient electron-hole pair separation for hydrogen evolution, *Angew. Chem. Int. Ed.* 55 (6) (2016) 2137–2141.
- [59] E.T. Yun, J.H. Lee, J. Kim, H.D. Park, J. Lee, Identifying the nonradical mechanism in the peroxymonosulfate activation process: singlet oxygenation versus mediated Electron transfer, *Environ. Sci. Technol.* 52 (12) (2018) 7032–7042.
- [60] Y. Yang, G. Banerjee, G.W. Brudvig, J.H. Kim, J.J. Pignatello, Oxidation of organic compounds in water by unactivated peroxymonosulfate, *Environ. Sci. Technol.* 52 (10) (2018) 5911–5919.
- [61] X.Y. Gao, X.C. Zhang, Y.W. Wang, S.Q. Peng, B. Yue, C.M. Fan, Rapid synthesis of hierarchical BiOCl microspheres for efficient photocatalytic degradation of carbamazepine under simulated solar irradiation, *Chem. Eng. J.* 263 (2015) 419–426.
- [62] W.H. Koppenol, D.M. Stanbury, P.L. Bounds, Electrode potentials of partially reduced oxygen species, from dioxygen to water, *Free Radical Bio. Med.* 49 (3) (2010) 317–322.
- [63] C. Lee, H.H. Kim, N.B. Park, Chemistry of persulfates for the oxidation of organic contaminants in water, *Membr. Water Treat.* 9 (6) (2018) 405–419.
- [64] L.M. Hu, G.S. Zhang, M. Liu, Q. Wang, P. Wang, Enhanced degradation of Bisphenol A (BPA) by peroxymonosulfate with Co₃O₄-Bi₂O₃ catalyst activation: effects of pH, inorganic anions, and water matrix, *Chem. Eng. J.* 338 (2018) 300–310.
- [65] H.Y. Dong, Z.M. Qiang, J.F. Lian, J.H. Qu, Degradation of nitro-based pharmaceuticals by UV photolysis: kinetics and simultaneous reduction on halonitromethanes formation potential, *Water Res.* 119 (2017) 83–90.
- [66] S.Y. Huang, C.C. Chen, H.Y. Tsai, J. Shaya, C.S. Lu, Photocatalytic degradation of thiobencarb by a visible light-driven MoS₂ photocatalyst, *Sep. Purif. Technol.* 197 (2018) 147–155.